



Contents lists available at ScienceDirect

Journal of Computational and Applied Mathematics

journal homepage: www.elsevier.com/locate/cam



Accuracy of the robust design analysis for the flux barrier modelling of an interior permanent magnet synchronous motor

Mihály Katona ^{*}, Miklós Kuczmann, Tamás Orosz

Department of Power Electronics and Electric Drives, Széchenyi István University, Egyetem tér 1., Győr, 9026, Hungary



ARTICLE INFO

Article history:

Received 5 October 2022

Received in revised form 1 March 2023

Keywords:

Electrical machines

Optimisation

Finite element method

Robust design analysis

Design of Experiment methods

ABSTRACT

Mass-produced electrical machines are subjected to manufacturing uncertainties in terms of geometry. A robust design is inevitable to ensure the consistent performance of the electric motor. Some parts of the rotor geometry are often simplified, like the flux barrier at the end of the magnets. This paper presents a design optimisation regarding the torque ripple and the average torque. The aim is to assess the effects of the flux barrier on the main properties of a permanent magnet synchronous motor. Also, robust design analysis is presented on the flux barrier. The computational burden of the robust design analysis is immense, even if uniform uncertainties are assumed. In this case, different Design of Experiment (DoE) methods reduce the number of simulations. The efficiency of the DoE methods is compared in terms of simulation number and extreme value approximation. We found that the Central Composite method is the most accurate, while the Plackett–Burman is the most efficient in this particular case.

© 2023 The Author(s). Published by Elsevier B.V. This is an open access article under the CC BY license (<http://creativecommons.org/licenses/by/4.0/>).

1. Introduction

Uncertainties can be identified in engineering tasks, such as material properties or manufacturing tolerances. Traditional engineering solves the problem of uncertainties by implementing safety factors [1]. It creates an over-designed product that is unacceptable in a competitive market, such as e-mobility. The market constantly pressures the industry to decrease the prices, keeping the performance of its products at least a consistent level. A robust design may be sub-optimal but keeps a firm consistency. It can also reduce manufacturing costs by reducing defective products because of the insensitivity to small changes in the applied materials. A new way of thinking shows that robustness is defined earlier during the design stage of the product [2]. However, considering the uncertainties during the early design stage can greatly increase the computational demand of the design process. This is a current problem in the industry, and research on how to create simple models which can consider the uncertainties during this early design stage and give reasonably accurate results with minimal computational demand [2]. In the case of Permanent Magnet Synchronous Motor (PMSM), one of the main arguments against utilising robust design optimisation in the early stage of the design is the huge computational burden [3]. A dramatic increase in the number of design cases is foreseeable to find the robust optima [4], but the rate of increase is rarely reported. For example: if only the impact of one uncertain parameter is considered, then two additional simulations are needed in the extreme values to assess the robustness. The situation in the case of a real scenario is much more complex, where the computational demand of considering the uncertainties can easily lead to tens or hundreds of times more simulations than the original process.

* Corresponding author.

E-mail address: katona.mihaly@sze.hu (M. Katona).

The goal of the paper is to investigate the possibilities for reducing the computational needs in terms of robust design analysis of a PMSM. There are possible approximations to minimise the computational burden. For example, to assume uniform uncertainties, meaning that the uncertainties are identical on each part of the motor. On the other hand, it is a simplification as it neglects the combinations of stochastic uncertainties [3]. Another possible solution to reduce the computational burden is to apply different DoE methods for robust design analysis [5,6]. Those provide an approximation of different levels to find the extreme values of the objective function and minimise the computational need by representing only a fraction of cases in the manufacturing tolerance range [7]. However, the DoE methods cause information loss, depending on the given problem. In the case of electrical machine analysis, some researchers used these methods previously to reduce the computational cost of their robust design analysis [6,8]. However, only some of them compared the performance of the different methods. Orosz et al. [9] presented a robust design analysis for a Brushless DC Electric Motor in the case of uniform uncertainties. This research aims to determine the worst-case scenario and the information loss of the DoE methods [5]. Different DoE methods were compared to the Full Factorial design results. It was found that the Central Composite method approximated precisely the minimum and the maximum deviation caused by the manufacturing tolerances, while the Plackett–Burman method overestimated and the Box–Behnken underestimated the results. Other possible solutions to reduce the computational burden of robust optimisation in the case of PMSM are presented in [3]. Yang et al. [3] applied the Worst Uncertain Combination Analysis to find the designs producing the worst case in terms of efficiency and torque ripple. Also, a new operation was proposed, the Parameter Rounding During the Calculation. The results show an 11% reduction in the computational burden. Considering a non-uniform-uncertainty model, Liu et al. [10] show that the uncertainty range and the sequence of the uncertainties also matter.

The subject of the paper is the Toyota Prius 2004 Interior Permanent Magnet Synchronous Motor (IPMSM) because its geometry and its measurements are openly accessible from several sources [11–15]. This electrical machine became the basis for several papers [16–18]. However, most of the proposed papers have not considered the role of the flux barriers. The report [19] contains the schematic of the stator and rotor. However, the magnets' slot and the flux barrier at the end of the magnets are not clearly defined. The document [20] presents a detailed schematic. Nevertheless, the dimensions of the flux barrier are missing or contradict each other. For the foregoing reasons, the openly accessible geometries are not identical. They contain some simplifications, most of which model the flux barrier differently, as shown in Fig. 1. Those approximate the flux barrier by a circle arc [11], by a triangle [16], or else [17].

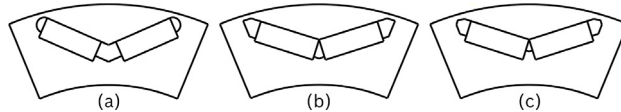


Fig. 1. Differently modelled flux barriers in the electromagnetic models of the Toyota Prius IPMSM machine (a): [11], (b): [12], (c): own model based on [19,20].

Simplifying the flux barrier and its changes in the manufacturing tolerance range can significantly affect the simulation results. The paper introduces a multi-objective optimisation without over-simplifying the shape to confirm the previous statement. The objectives are to minimise the torque ripple and maximise the average operational torque (AOT). Ge et al. [21] also optimised the geometry of a flux barrier to reduce the noise of an IPMSM. They applied only a minimal modification to the flux barrier, and a reduction of 26.79% was achieved in the torque ripple. The present paper aims to show the computational time and accuracy difference between different DoE methods on an optimised flux barrier geometry. The structure is as follows: the numerical model of the examined electric motor is described in Section 2.1. The proposed FEM model is validated by measurements and other openly accessible simulations in Section 2.2. The sensitivity of the applied mesh on the main parameters is analysed in Section 2.3. Section 3.1. describes the details of the optimisation process. The robust design analysis and different DoE methods are presented in Section 3.2. Section 4. contains the results of the simulations. Section 5. discusses the optimal design and compares the different DoE methods.

2. Modelled geometry and validation

2.1. Geometry

Fig. 2 presents the created parametric flux barrier geometry, where the constant parameters came from the available data. A detailed description of the whole motor model is published in [22]. The subjects of the optimisation and robust design analysis are the geometrical changes of the flux barrier. The values of the parameters are summarised in Table 1. Fig. 2 (a) presents the measures, which dimensions based on the previously published data [20], where parameter A and L_{56} are not defined. The presented model does not take the value of L_{36} into consideration directly, to slightly reduce the complexity and numeracy of the variables. Therefore, L_{36} and L_{46} parameters are defined by Eqs. (2) and (3). This way the β_2 and β_3 angles are fixed in Fig. 2 (b). Parameter A was chosen for the optimisation. In Fig. 2 (c) the parameters non-dependent on parameter A are depicted, besides in Fig. 2 (d) the dependent parameters are shown. The relations of β_4 and β_5 to parameter A are defined in Eqs. (4) and (5).

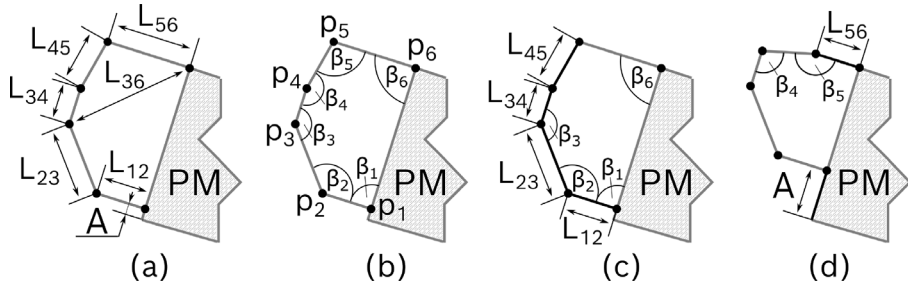


Fig. 2. Parameterisation of the flux barrier where (a) defines the lines, (b) defines the angles and vertices, (c) presents the fixed values and (d) shows the variables.

Table 1

Parameters and values of the flux barrier.

Lines	Value [mm]	Type	Angles	Values [deg]	Type
A	[0.5..3.0]	Optimised	β_1	90.0	Fixed
L_{12}	2.10	Fixed	β_2	129.1	Fixed
L_{23}	3.02	Fixed	β_3	141.2	Fixed
L_{34}	1.50	Fixed	β_4	[85.0..167.8]	Variable
L_{45}	2.20	Fixed	β_5	[102.2..189.2]	Variable
L_{56}	[1.80..3.53]	Variable	β_6	90.0	Fixed

$$L_{56} = 4 - \sqrt{4.84 - (2.65 - A)^2} \quad (1)$$

$$L_{36} = \sqrt{(16 - (4.15 - A)^2)} \quad (2)$$

$$L_{46} = \sqrt{(16 - (2.65 - A)^2)} \quad (3)$$

$$\beta_4 = \begin{cases} \cos^{-1}((L_{56}^2 - L_{46}^2 - 4.84)/(-9.68 \cdot L_{46})) & \text{if } 0.5 \leq A \leq 2.6 \\ + \cos^{-1}((L_{36}^2 - L_{46}^2 - 2.25)/(-5.5 \cdot L_{46})) & \text{if } 2.6 < A \leq 3.0 \end{cases} \quad (4)$$

$$\beta_5 = \begin{cases} \cos^{-1}((L_{46}^2 - L_{56}^2 - 4.84)/(-4.4 \cdot L_{56})) & \text{if } 0.5 \leq A \leq 2.6 \\ 360 - \cos^{-1}((L_{46}^2 - L_{56}^2 - 4.84)/(-4.4 \cdot L_{56})) & \text{if } 2.6 < A \leq 3.0 \end{cases} \quad (5)$$

First-order elements create the presented approximation of the flux barrier as the FEMM [23] can only utilise this kind of geometry. Furthermore, the documentation does not indicate that the flux barrier is designed and manufactured using higher-order elements like splines. The material properties and any additional information to create the model are from [11,17]. The Digital-Twin-Distiller (DTD) used in the present paper provides an environment for optimisation, and robust design analysis [9].

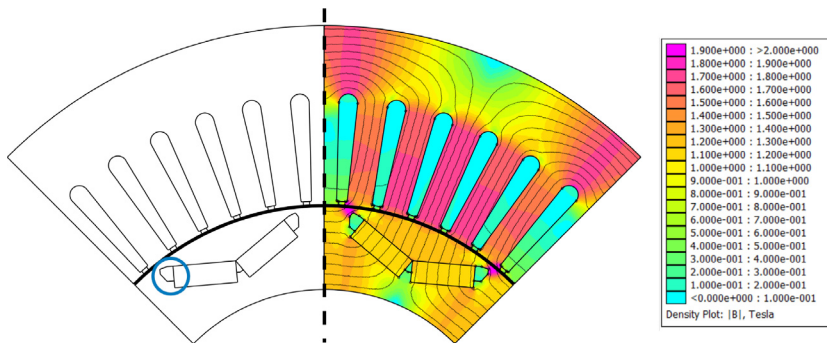


Fig. 3. The left side of the picture shows one pole of modelled 2D geometry, while the right side shows the flux distribution in the selected pole segment at $i = 250$ A.

The zoom-in in Fig. 4 depicts the different possibilities for p_2 to p_5 vertices if uncertainties are considered. The uncertainties are in the manufacturing tolerance range as $\delta_i, \delta_j \in [-0.06, 0, 0.06]$. Those define nine discrete cases per vertex in the direction of x' and y' . There is a shift in the axes to the horizontal and vertical positions. The angle shift is defined as $x' \angle x' | \zeta = 17.5^\circ$. Later on the optimisation defines the value of parameter A , thus fixing the geometry of the flux barrier. After that, during the robust design analysis the vertices are shifted to a corresponding discrete point creating different cases defined in Section 3.2. The coordinates of the discrete points are calculated as:

$$(x'_{pn}, y'_{pn}) = (x'_{pn} + \delta_i, y'_{pn} + \delta_j) \mid n \in [2..5], \delta_i, \delta_j \in [-0.06, 0, 0.06] \quad (6)$$

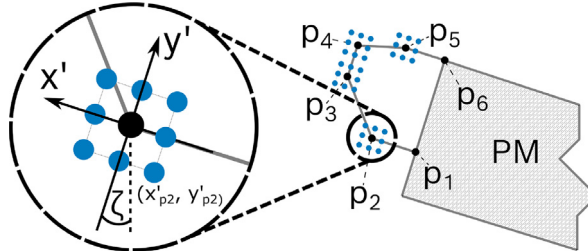


Fig. 4. The zoom-in of the flux barrier is the parameterisation for the robust design analysis.

2.2. Validation

Fig. 5(a) compares the results of the DTD 2D model that depicts one pole of the electric motor shown in Fig. 3 to the solution of a different software environment presented in [11]. The full model marks the result of the whole motor model and the pole model means a partial model as shown in Fig. 3 but coded in Matlab environment [11]. The FEM solver was FEMM in both cases. The cogging torque curves show no significant difference that confirms the accuracy of the created code in DTD environment [18].

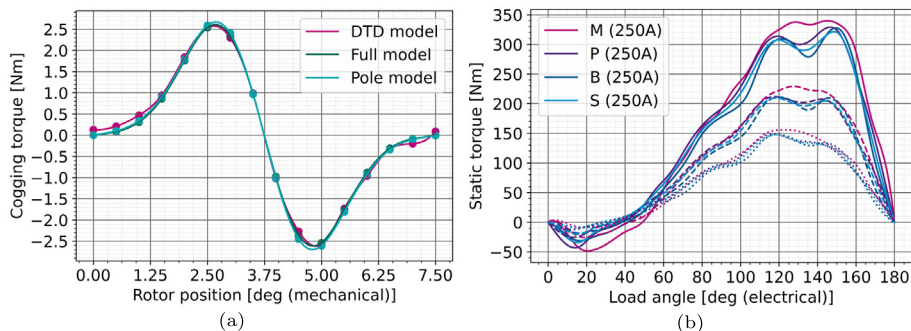


Fig. 5. (a) comparison of the cogging torque in different software environments, (b) comparison of the static torque to the manufactured Toyota Prius 2004 motor measurements with different flux barrier geometries M : measurement [15], B : AP [11], P : Pyleecan [12], S : DTD [22], the dashed line presents the values at 150 A, and the dotted line at 100 A.

Meanwhile, Fig. 5(b) gives the comparison of different flux barrier geometries [11,12] depicted in Fig. 1 created in DTD software environment and the measurement data from [20]. The simulations follow the circumstances of the measurement presented in [15]. There is a difference at high currents between the measurement and simulation data in the vicinity of the maximum torque. That is possibly the cause of the different degrees of the slotting effect [17], and the uncertainties of the winding pattern [22]. The results show a significant correlation that confirms the accuracy of the created code.

2.3. Mesh sensitivity

This investigation aims to show that the effect of the mesh density in the flux barrier is incomparable to the effect of the parameter A and to find the coarsest reasonable mesh to minimise the computational demand. To describe a given complex geometric element in a well-approximated way by its finite element mesh, the refining the finite element mesh is required to a certain extent. The mesh density affects the numerical error, computational needs, and time required for the simulation. The finite element mesh size (h) assigned to each material in the simulations is a fixed value except the air assigned to the flux barrier. The mesh size definition used in FEMM is described in [23]. During the analysis of the mesh sensitivity, the mesh size of the flux barrier varies in $h_{fb} \in [0.025, 0.05, 0.1, 0.25, 0.4, 0.55, 0.7, 0.85, 1]$ shown in Fig. 6.

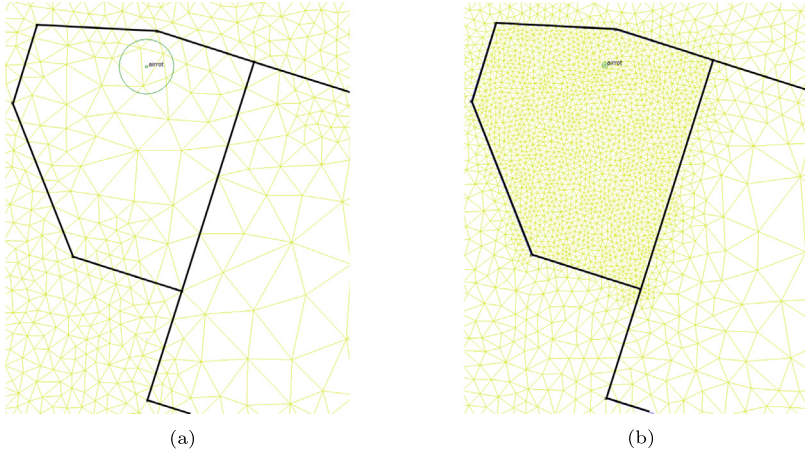


Fig. 6. (a) The finite element mesh at $h_{fb} = 1$ and (b) the finite element mesh at $h_{fb} = 0.1$.

A Full Factorial investigation provides the data for the mesh sensitivity analysis as written in Section 3.1. Fig. 7 shows the number of nodes for different mesh sizes. Significant growth can be seen after $h_{fb} = 0.25$ in the number of nodes and computational cost. The simulations for $h_{fb}(x) = \{0.1 + 0.15x \in [0..6]\}$, that means 399,672 cases approximately required the same amount of time as $h_{fb} = \{h_{fb} \in [0.025, 0.05]\}$ of 114,192 simulations. Fig. 8 shows the probability density of the difference in AOT (dif) for every mesh density (h_{fb}):

$$dif = f_{AOT}(A_j, \varrho_k, 1, i_n) - f_{AOT}(A_j, \varrho_k, h_{fbm}, i_n), \text{ where}$$

$$j \in [1..26], k \in [1..9], m \in [2..9], n \in [1..4] \quad (7)$$

where AOT depends on the flux barriers shape denoted by (A), the load angle (ϱ), the mesh size (h_{fb}) and the load current (i). Eq. (7) defines the AOT difference in every 7488 similar simulation cases defined by A ϱ , h_{fb} and i where the $h_{fb} \neq 1$ to $h_{fb} = 1$.

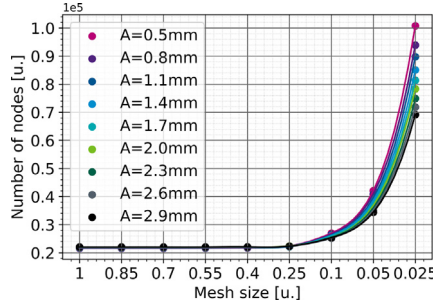


Fig. 7. The number of nodes in the discretised motor segment for different mesh sizes.

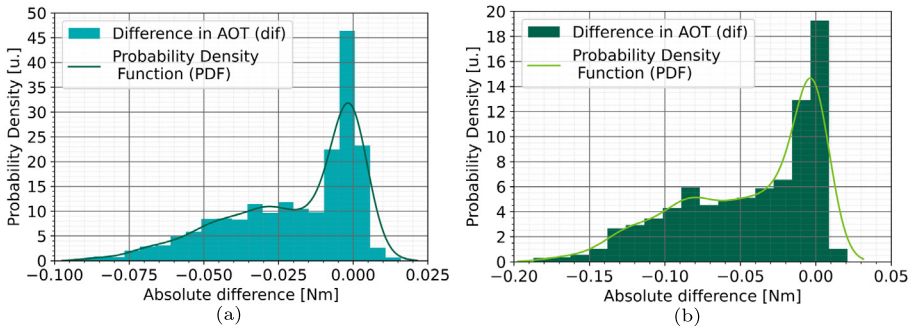


Fig. 8. Probability density of the torque difference (a): 100 A, (b): 250 A.

The optimal width of the bins for different currents was calculated by the Freedman–Diaconis rule [24]. This rule defines the optimal bin width for a minimal integrated mean squared error [25]. In Eq. (8) the IQR denotes the Interquartile

Range [26], x is the different entries of the data set and num is the number of entries. The Eq. (9) defines the optimal number of bins:

$$w_{bin} = 2 \frac{IQR(x)}{\sqrt[3]{num}} \quad (8)$$

$$n_{bin} = \frac{\max(x) - \min(x)}{w_{bin}} \quad (9)$$

The statistical function package of Scipy [27] provides the Probability Density Function by using Gaussian Kernel Density Estimation. In Fig. 8 the PDF means that its integral in a discrete range gives the probability that the given variable falls in the defined range. The absolute difference points out that there is a 100% probability that the results deviate only in the range of $[-0.20..0.025]$ Nm]. In the worst case, it means approximately 0.15% of difference in the torque estimation. This difference was deemed to be negligible compared to the effect of parameter A . It can be stated that the mesh size of the flux barrier $h_{fb} = 1$ is sufficient for the robust design analysis.

3. Calculations

3.1. Design optimisation

The design optimisation aims to minimise the torque ripple and to maximise the average operational torque (AOT). The optimised variable is parameter A based on Section 2.1. The basis of the comparison is the possible maximal AOT related to the load angle (ϱ) at different currents (i). The torque ripple is analysed at the load angle corresponding to the possible maximal AOT. The mesh size (h_{fb}) does not affects the results significantly as presented in Section 2.3. Although, Fig. 12 shows that a lower AOT and torque ripple value may appear as the mesh becomes denser. If the torque ripple is marked by (rip), and the optimal design is (opt), then:

$$opt = f(\min(g_{rip}(A, \varrho, h, i)), \max(g_{AOT}(A, \varrho, h, i))) \quad (10)$$

The goal is to understand how the flux barrier geometry affects the maximum of the AOT and the torque ripple. The Full Factorial of every possible case provides the data for the design optimisation as in mesh sensitivity analysis. The parameter $A = \{0.1A | A \in [5..30]\}$ in millimetres creates 26 different design. The load angle varies in $\varrho = \{4\varrho | \varrho \in [29..37]\}$ in electrical degrees. The load angle is the angular difference between the stator flux vector (φ) and the pole flux vector of the rotor. Every design requires nine simulations to get a static torque diagram as the stator flux vector is non-variable [22]. The torque ripple was evaluated in 61 different positions of the co-rotating system to calculate the AOT for every given load angle. In a co-rotating system the rotor position (γ) in mechanical degrees is $\gamma(\varrho, x) = \{\varrho + 0.25x | x \in [0..60]\}$. Simultaneously, the flux vector angle of the stator is in $\varphi = \{\varphi \in [0..60]\}$ in electrical degrees. The geometry was simulated on four different currents $i = \{50i | i \in [2..5]\}$ and on nine possible mesh sizes of $h_{fb} = \{h_{fb} \in [0.025, 0.05]\}$ plus $h_{fb}(x) = \{0.1 + 0.15x \in [0..6]\}$. That means a Full Factorial of $26 \cdot 9 \cdot 61 \cdot 4 \cdot 9 = 513864$ simulations and 8424 entries of the torque ripple and the AOT to evaluate. As one simulation runs for approximately 25 s and with the eight parallel processes possible with the available computing power, the optimisation process took 18 days and 14 h to simulate.

3.2. Robust design analysis

The different DoE methods help to ease the computational burden and to determine how robust the selected design is. During the robust design analysis the input variables are the four vertices of the flux barrier (p_i), where $p_i = (x_i, y_i) | i = [2..5]$ coordinates. Fig. 4 presents the parameterisation of the flux barrier for the robust design analysis. The coordinates of vertices vary in two directions of x' and y' presented in Section 2.1. This creates eight variables deemed as the factors (n) of the DoE methods. Any variable falls in a discrete range of 3 values described by $\delta_i, \delta_j \in [-0.06, 0, 0.06]$. Those are the levels (m) of the DoE methods. The measurement of a manufactured motor design provides the basis for the discrete tolerance range. The uncertainties are assumed to be uniform, following the definition of [28]. That means that the modification on each pole is the same. To calculate the AOT and to precisely compare the results, the same co-rotating system were defined where the rotor position is $\gamma(138.5, x) = \{138.5 + 0.25x | x \in [0..60]\}$ and the angle of the stator flux vector is $\varphi = \{\varphi \in [0..60]\}$. This creates 61 different simulations to define the AOT of one design for any case of robust design analysis.

This paper investigates the Fractional Factorial, the Box-Behnken, Plackett-Burman and Central Composite methods. The robust design analysis aims to assess the error of the uncertain cases to the optimal design at the peak of AOT of the optimum $A = 2.1$ mm design. Section 5.1 contains the details of this decision. Fig. 9 presents the similarities of different DoE methods. The Central Composite shadows all the Fractional Factorial cases and the Plackett-Burman design. Furthermore, there is only one common case between the Central Composite and the Box-Behnken methods.

Full Factorial (FF): All the possible variables of the design parameters, so-called factors and those number of possible values, called levels, are simulated [29]. In this case, eight factors and three levels create $m^n = 3^8 = 6561$ different cases.

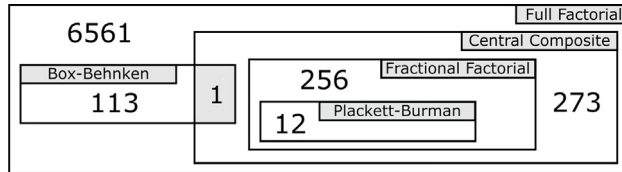


Fig. 9. The similarities of different DoE methods in the number of design cases.

Furthermore, $6561 \cdot 61 = 400221$ simulations calculate the torque ripple at the peak of AOT as presented in Section 3.1. This number of simulations is a considerable burden to run in terms of simulation time. One simulation takes 25 s to finish on the available computer, and eight processes run parallel. The Full Factorial design takes approximately 14 days and 11 h to calculate.

Fractional Factorial (FrF): If only the minimum and the maximum of the $\delta_i, \delta_j \in [-0.06, 0, 0.06]$ range is taken into consideration, then it can be defined as hyper-rectangle. It can be assumed that the furthest values from the optimum are in the vertices of the data set. However, it cannot be guaranteed that the worst case is located in the vertices [30]. To examine the defined Fractional Factorial design, $m^n = 2^8 = 256$ cases and 15,617 simulations run for approximately 13.5 h.

Box-Behnken (BB): This method does not utilise any part of the Fractional Factorial design. It is rotatable as there are three levels for each factor, and it is generally used for more than two factors [29]. It creates 113 cases and 6893 simulations that take approximately 6 h to run.

Plackett–Burman (PB): It is a modified Fractional Factorial design, where the relations between different factors are ignored. Fewer experiments are enough than the other DoE methods to calculate the significant effects [5,29]. It defines 12 cases and 732 simulations that run for 40 min.

Central-Composite (CC): A version of response surface design that utilises Fractional Factorial design also. Centre points are also added to the calculations [29]. It creates 273 cases and 16,653 different simulations that last 14.5 h to finish.

4. Results

4.1. Design optimisation

The following figures show the torque of the $A = 2.1$ mm, $h = 1$ design as in [18] is an optimal design for cogging torque. In Fig. 10(a) the AOT range of every possible solution is presented for 250 A. The envelope curves represent the maximum and the minimum of every possible solution for the given load angle. The mean curve is calculated from every possible solution. In Fig. 10(b) the maximum of the AOT is presented for every design created by parameter A. The upper envelope curves approximate the lowest and the highest simulated values by the variation of the mesh size.

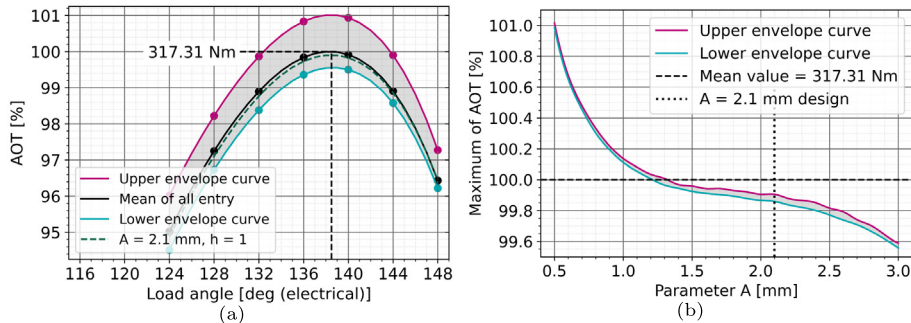


Fig. 10. (a): The AOT as a function of the load angle and (b): maximum of the AOT as a function of parameter A.

Fig. 11(a) contains the amplitude of the torque ripple. In this case, the amplitude is the difference between the average and maximum of the torque ripple. The load angle belonging to the maximum of the AOT is also presented. In Fig. 11(b) the maximum AOT's torque ripple is depicted for every design defined by parameter A.

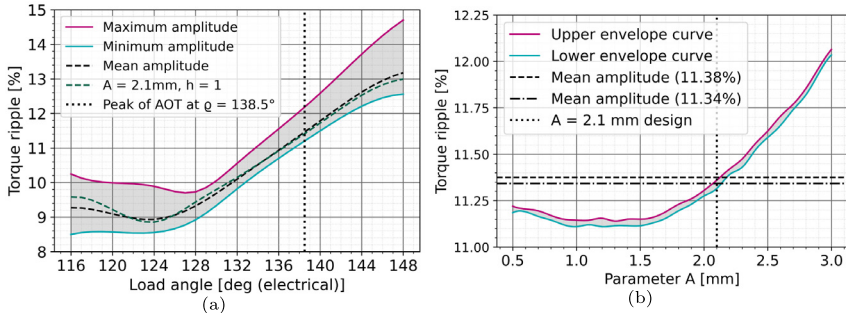


Fig. 11. Amplitude of the torque ripple (a): for every design (b): in the case of $\varrho = 138.5^\circ$.

In Fig. 12 the objective functions are presented, namely the torque ripple to the maximum of the AOT. The design of $A = 2.1\text{ mm}$ is also presented in the case of coarse and fine mesh.

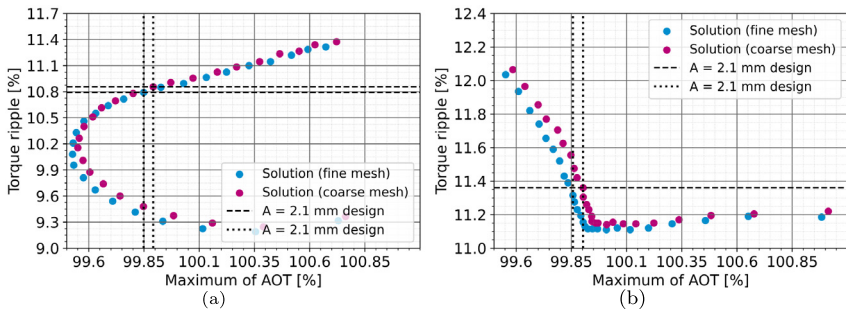


Fig. 12. Comparison of the objectives (a): 100 A (b): 250 A.

4.2. Robust design analysis

Fig. 13 shows the distribution of the torque ripple affected by the geometrical uncertainties for different DoE methods to the original design.

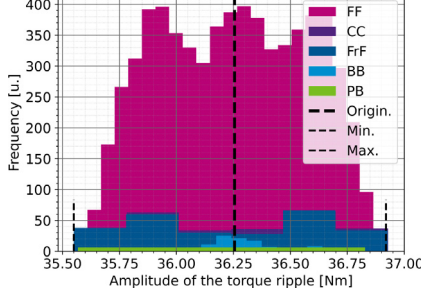


Fig. 13. Comparison of the different DoE methods for the torque ripple, where the amplitude of the original optimised model's torque ripple is 36.25 Nm, the minimum of the robust design analysis is 35.55 Nm and the maximum is 36.92 Nm.

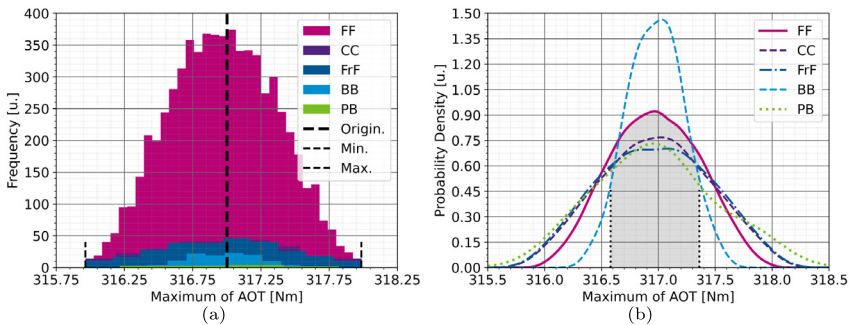


Fig. 14. Comparison of the DoE methods for AOT (a): frequency, where the maximum AOT of the original optimised model is 317.02 Nm, the minimum of the robust design analysis is 315.96 Nm and the maximum is 317.99 Nm (b): probability density.

Fig. 14(a) contains the same representation as in Fig. 13 but for the maximum of the AOT. The Fig. 14(b) provides the probability density functions of different DoE methods in terms of AOT affected by the geometrical uncertainties.

5. Discussion

5.1. Design optimisation

Fig. 10(a) shows that the shape of the flux barrier defined by the parameter A significantly affects the AOT. The AOT varies by more than 1.5%. This means that the shape and size of the flux barrier are non-negligible, and it is not worth simplifying it. Further simulation data shows that the current also affects the peak position of the AOT defined by the load angle. It increases by 8° from 100 A to 250 A. This way, the stable working range also widens. In **Fig. 10(b)** the maximum torque of the design $A = 2.1$ mm falls in a range close to the mean value. It shows that the mesh size is also insignificant, but its effect is higher in the case of $A > 1.2$ mm. As the parameter A increases, the magnetic bridge between the flux barrier and the air gap becomes narrow. High currents cause saturation of those parts and a reduction in the output torque. **Fig. 11(a)** shows that the load angle significantly affects the torque ripple. As the load angle increases, the torque ripple also increases. **Fig. 11(b)** presents that the growth of parameter A also increases the torque ripple.

Fig. 12 shows that the optimal solution for the objective functions may be near the lower right side of the diagram. There are not many possible options fulfilling this criterion. It was found that the higher the maximum of the AOT, the lower the parameter A is. The paper [18] shows that the lower the value of parameter A , the higher the cogging torque becomes. This creates a contradiction between the objectives of the design optimisation. The design $A = 2.1$ mm can be an optimal solution for multi-objective optimisation. For the robust design analysis, this design provides the basis.

5.2. Robust design analysis

The robust design analysis finds the worst possible cases, namely the minimum and the maximum deviation from the optimal design. In **Fig. 13** the torque ripple deviates approximately by $[-0.70 \text{ Nm}, +0.67 \text{ Nm}]$. This results from the Full Factorial design, Fractional Factorial and Central Composite design. The Central Composite design contains all the Fractional Factorial cases. However, the CC does not seem to contribute to the extrema over FrF . The Fractional Factorial design contains all the cases of the Plackett–Burman method. As **Fig. 13** shows, in terms of simulation number and extremum mapping, the PB is the most efficient with the difference from the original of $[-0.69 \text{ Nm}, +0.58 \text{ Nm}]$ calculated by 12 cases. The Box–Behnken design has only one similar case to the Central Composite design. In terms of searching for the limits, it is the least efficient. It has more than nine times more cases than the PB and only shows the extreme values at $[-0.48 \text{ Nm}, 0.52 \text{ Nm}]$. It is also important to note that the differences between the results of the DoE methods are comparable to the mesh sensitivity. In **Fig. 14(a)** the same frequency distribution is presented as in **Fig. 13** but for the maximum of AOT. The results are compared in **Table 2**.

Fig. 14(b) contains the probability density of the AOT. The maximal negative deviation from the mean value is 315.96 Nm. The maximal positive deviation is 317.99 Nm. The mean value of the Full Factorial data set is 316.97 Nm. The standard deviation for the Full Factorial data set is $\sigma = 0.39$ Nm. Suppose the frequency of the calculated results correlates with the possibility of the manufactured results. In this case, the possibility that the maximum of the AOT falls in the range of $[mean(FF) - \sigma, mean(FF) + \sigma]$ is the following. The possibility of $P([mean(FF) - \sigma \leq AOT \leq mean(FF) + \sigma])$ is presented in **Table 2**. Integrating the Probability Density Function on a discrete range of $[mean(FF) - \sigma, mean(FF) + \sigma]$ gives the results. The results show that the CC , FrF and PB underestimate the FF result, on the other hand, the BB method seems to overestimate it significantly.

Table 2
Results of the robust design analysis: Difference, possibility and case numeracy.

DoE	Torque ripple [Nm]	AOT [Nm]	$AOT \in [FF \pm \sigma]$	Cases [u.]
FF	[-0.70..+0.67]	[-1.00..+0.98]	64.58%	6561
CC	[-0.70..+0.67]	[-1.00..+0.98]	55.00%	273
FrF	[-0.70..+0.67]	[-1.00..+0.98]	52.50%	256
BB	[-0.48..+0.52]	[-0.58..+0.54]	87.06%	113
PB	[-0.69..+0.58]	[-0.79..+0.80]	50.94%	12

The Fractional Factorial and Central Composite methods accurately approximate the Full Factorial design in terms of extreme values. The probability results show that the Plackett–Burman method approximates the Fractional Factorial and Central Composite methods most efficiently in terms of simulation number, but also overestimates the Full Factorial results. The Box–Behnken method significantly deviates from the other three methods.

6. Conclusion

The present paper examined the role of the flux barrier on the main parameters of an IPMSM machine. The shape of this flux barrier geometry is modelled by four dependent and one independent point. The dependent parameters can be derived from the independent point, parameter A . The value of parameter A resulted from an optimisation process, where the goals were to reduce cogging torque, the torque ripple and maximise the average operational torque (AOT). The shape of the resulting geometry was validated on previously published measured and simulated values of the Toyota

Prius 2004 electric motor. The simple three-level Full Factorial robust design analysis of the considered eight factors creates 6561 cases. Considering the impact of the flux barrier shape is a huge computational burden during the early design stage of an electrical machine. This investigation used different Design of Experiment methods (Plackett–Burman, Central Composite Design, Box–Behnken and Fractional Factorial Design) and compared their accuracy and efficiency. The analysis implies that it is worth considering a mesh sensitivity analysis for robust design calculations. The reduction in the number of simulations because of the DoE methods may counterweight the computational time needs of the denser mesh. To conclude, the Plackett–Burman method is the most efficient and reasonably accurate for robust design calculations in this research. This methodology increases the computational demand about 12 times the optimisation process. In contrast, the other methodologies need more than hundreds of calculations to estimate the maximum error of a uniform uncertainty design. However, the Central Composite design is more accurate. As the greatest possible difference is less than approximately 0.5% to the results of the original design, it can be stated that the design is robust in the range of manufacturing tolerances. Still, the effects of the uncertainties on the flux barrier are not negligible. The data and the code created for this research are available at <https://github.com/KatonaMihaly/ESCO2022>.

CRediT authorship contribution statement

Mihály Katona: Conceptualization, Methodology, Software, Validation, Investigation, Data curation, Writing – original draft, Visualization, Funding acquisition. **Miklós Kuczmann:** Writing – review & editing, Supervision. **Tamás Orosz:** Conceptualization, Methodology, Software, Data curation, Writing – review & editing, Supervision.

Data availability

The Github repository containing the data/code is cited in the paper and also CRedit form.

Acknowledgements

The authors would like to express their gratitude to the help of Vilmos Paiss, András Bolyog and János Füzesi for sharing their knowledge in this research field; furthermore, Attila Geleta and Csongor Horváth for the help in the funding of this project. This research was funded by the project 2020-2.1.1-ED-2020-00062 Establishment of Electromobility Development Center at Robert Bosch Kft. - Phase 1.

References

- [1] P. Koch, et al., Design for six sigma through robust optimization, *Struct. Multidiscip. Optim.* 26 (2004) 235–248, <http://dx.doi.org/10.1007/s00158-003-0337-0>.
- [2] S. Goetz, et al., Early robust design—Its effect on parameter and tolerance optimization, *Appl. Sci.* 11 (20) (2021) <http://dx.doi.org/10.3390/app11209407>.
- [3] Y. Yang, et al., Methods to reduce the computational burden of robust optimization for permanent magnet motors, *IEEE Trans. Energy Convers.* 35 (4) (2020) 2116–2128, <http://dx.doi.org/10.1109/TEC2020.3016067>.
- [4] J.-G. Lee, et al., Robust optimization approach applied to permanent magnet synchronous motor, *IEEE Trans. Magn.* 53 (6) (2017) 1–4, <http://dx.doi.org/10.1109/TMAG.2017.2662740>.
- [5] F. Jurecka, *Robust design optimization based on metamodeling techniques* (Ph.D. thesis), Technische Universität München, 2007.
- [6] G. Bramerdorfer, et al., Modern electrical machine design optimization: Techniques, trends, and best practices, *IEEE Trans. Ind. Electron.* 65 (10) (2018) 7672–7684, <http://dx.doi.org/10.1109/TIE.2018.2801805>.
- [7] P. Maussion, Design of experiments in electrical engineering: Applications in control and modeling, in: 2017 IEEE Workshop on Electrical Machines Design, Control and Diagnosis, WEMDCD, 2017, pp. 179–186, <http://dx.doi.org/10.1109/WEMDCD.2017.7947744>.
- [8] G. Bramerdorfer, Computationally efficient tolerance analysis of the cogging torque of brushless PMMSMs, *IEEE Trans. Ind. Appl. PP* (2017) 1, <http://dx.doi.org/10.1109/TIA.2017.2682797>.
- [9] T. Orosz, et al., Automatic tolerance analysis of permanent magnet machines with encapsulated FEM models using digital-twin-distiller, *Processes* 9 (11) (2021) <http://dx.doi.org/10.3390/pr9112077>.
- [10] H. Liu, et al., A permanent magnet assembling approach to mitigate the cogging torque for permanent magnet machines considering manufacturing uncertainties, *Energies* 15 (6) (2022) <http://dx.doi.org/10.3390/en15062154>.
- [11] AP, Phd engineering electromagnetics, 2018, URL <http://phdengineeringem.blogspot.com/>. (Accessed 30 September 2022).
- [12] EOMYS, Pyleecan, 2020, URL <https://github.com/Eomys/pyleecan/tree/master/Tests/Data>. (Accessed 30 September 2022).
- [13] M. Katona, ESCO2022, 2022, URL <https://github.com/KatonaMihaly>. (Accessed 30 September 2022).
- [14] J.S. Hsu, et al., Report on Toyota/Prius Motor Design and Manufacturing Assessment, Oak Ridge National Laboratory, 2004, ORNL/TM-2004/137.
- [15] J.S. Hsu, et al., Report on Toyota/Prius Motor Torque Capability, Torque Property, No-Load Back Emf and Mechanical Losses - Revised 2007, Oak Ridge National Laboratory, 2007, ORNL/TM-2004/185.
- [16] D.G. Dorrell, et al., Analysis and design techniques applied to hybrid vehicle drive machines—Assessment of alternative IPM and induction motor topologies, *IEEE Trans. Ind. Electron.* 59 (10) (2012) 3690–3699, <http://dx.doi.org/10.1109/TIE.2011.2165460>.
- [17] V. Kuptsov, et al., Electromagnetic analysis and design methodology for permanent magnet motors using motoranalysis-PM software, *Machines* 7 (4) (2019) <http://dx.doi.org/10.3390/machines7040075>.
- [18] M. Katona, et al., Cogging torque analysis of Toyota Prius 2004 IPMSM motor with the digital-twin-distiller, in: Vehicle and Automotive Engineering 4, vol. 4, 2023, pp. 126–138, http://dx.doi.org/10.1007/978-3-031-15211-5_11.
- [19] J.S. Hsu, et al., Report on Toyota Prius Motor Thermal Management, Oak Ridge National Laboratory, 2005, ORNL/TM-2005/33.
- [20] T.A. Buress, et al., Evaluation of the 2007 Toyota Camry Hybrid Synergy Drive System, Oak Ridge National Laboratory, 2008, ORNL/TM-2007/190.
- [21] H. Ge, et al., Optimising the flux barriers of interior permanent magnet machine for noise reduction under certain load conditions, *IET Electr. Power Appl.* 15 (11) (2021) 1512–1528, <http://dx.doi.org/10.1049/elp2.12115>.

- [22] M. Katona, T. Orosz, Locked-rotor analysis of a Prius 2004 IPMSM motor with digital-twin-distiller, in: 2022 IEEE 20th International Power Electronics and Motion Control Conference, PEMC, pp. 201–208, <http://dx.doi.org/10.1109/PEMC51159.2022.9962847>.
- [23] D. Meeker, Finite element method magnetics, 2022, URL <https://www.femm.info/wiki/HomePage>. (Accessed 30 September 2022).
- [24] D. Freedman, P. Diaconis, On the histogram as a density estimator: L₂ theory, *Z. Wahrscheinlichkeitstheorie Verw Gebiete* 57 (4) (1981) 453–476.
- [25] K.H. Knuth, Optimal data-based binning for histograms, 2013, [arXiv:physics/0605197](https://arxiv.org/abs/physics/0605197).
- [26] F.M. Dekking, et al., A Modern Introduction to Probability and Statistics, Springer London, 2005, <http://dx.doi.org/10.1007/1-84628-168-7>.
- [27] P. Virtanen, et al., SciPy 1.0: Fundamental algorithms for scientific computing in Python, *Nature Methods* 17 (2020) 261–272, <http://dx.doi.org/10.1038/s41592-019-0686-2>.
- [28] Y. Yang, et al., A method for evaluating the worst-case cogging torque under manufacturing uncertainties, *IEEE Trans. Energy Convers.* 35 (4) (2020) 1837–1848, <http://dx.doi.org/10.1109/TEC2020.2996098>.
- [29] A.K. Das, S. Dewanjee, Chapter 3 - Optimization of extraction using mathematical models and computation, in: Computational Phytochemistry, Elsevier, 2018, pp. 75–106, <http://dx.doi.org/10.1016/B978-0-12-812364-5.00003-1>.
- [30] G. Steiner, et al., Managing uncertainties in electromagnetic design problems with robust optimization, *IEEE Trans. Magn.* 40 (2) (2004) 1094–1099, <http://dx.doi.org/10.1109/TMAG.2004.824556>.